Carbon 157 (2020) 97–105

Contents lists available at ScienceDirect

Carbon

journal homepage: www.elsevier.com/locate/carbon

Orders of magnitude reduction in the thermal conductivity of polycrystalline diamond through carbon, nitrogen, and oxygen ion implantation

Ethan A. Scott [a], Khalid Hattar [b], Jeffrey L. Braun [a], Christina M. Rost [a], John T. Gaskins [a], Tingyu Bai [c], Yekan Wang [c], Claire Ganski [c], Mark Goorsky [c], Patrick E. Hopkins [a, d, e, *]

[a] Department of Mechanical and Aerospace Engineering, University of Virginia, Charlottesville, VA, 22904, USA
[b] Sandia National Laboratories, Albuquerque, NM, 87185, USA
[c] Materials Science and Engineering, University of California Los Angeles, Los Angeles, CA, 90095, USA
[d] Department of Material Science and Engineering, University of Virginia, Charlottesville, VA, 22904, USA
[e] Department of Physics, University of Virginia, Charlottesville, VA, 22904, USA

ARTICLE INFO

Article history:
Received 8 July 2019
Received in revised form
20 September 2019
Accepted 25 September 2019
Available online 28 September 2019

ABSTRACT

Despite the exceptional thermal and mechanical functionalities of diamond, its superlative properties are highly subject to the presence of point defects, dislocations, and interfaces. In this study, polycrystalline diamond is ion implanted with C^{3+}, N^{3+}, and O^{3+} ions at an energy of 16.5 MeV, producing an amorphous layer at the projected range and a damaged crystalline region between the surface and amorphous layer. Using time-domain thermoreflectance in combination with thermal penetration depth calculations based upon the multilayer heat diffusion equation, it is determined that reductions in the thermal conductivity can span nearly two orders of magnitude while still maintaining a polycrystalline structure within the regions thermally probed. Dynamical diffraction simulations of high-resolution x-ray diffraction measurements demonstrate the formation of a strained layer localized at the end of range, with much lower levels of strain near the surface. Furthermore, within the polycrystalline region above the amorphous layer, the average number of displacements-*per*-atom from the ion irradiation is found to be $<1\%$, with mass impurity concentrations much less than 1%. These low defect concentrations within the thermally probed region demonstrate the remarkably large impact that dilute levels of defects from the ion implantation can have on the thermal conductivity of diamond.

1. Introduction

Diamond has long been used in industrial applications due to its superlative elastic modulus, hardness, and heat dissipation properties. As power density requirements in modern electronics continue to grow, researchers have become increasingly interested in diamond for heat sink applications for high power amplification and radio-frequency electronic applications, for example, AlGaN and GaN-on-diamond devices [1,2]. Since their introduction in 2007 [3], GaN-on-diamond composite wafers have demonstrated superior thermal dissipation capabilities over silicon and SiC counterparts [4,5], enabling enhanced efficiency and significant reduction in device size. The property most critical for these performance increases is high substrate thermal conductivity, which, for single crystal diamond, is in excess of 2000 $W\,m^{-1}\,K^{-1}$ at room temperature [6,7]. The thermal conductivity, however, is highly sensitive to purity [8–10], which may be dependent on manufacturing and device integration processes that yield defects in the material, serving as phonon scattering sites.

In this study, we investigate phonon scattering induced via ion implantation, as it provides for a controlled means of altering thermal conductivity through disorder [11]. We implant polycrystalline substrates with ions of C^{3+}, N^{3+}, and O^{3+} at a beam energy of 16.5 MeV and fluences ranging from 4×10^{14} to $4\times10^{16}\,cm^{-2}$. Beyond industrial application, the insight gained through ion implantation studies provides an opportunity to explore new avenues in defect physics. For example, this ability to control the mass of the implant ion at a given energy and fluence

* Corresponding author. Department of Mechanical and Aerospace Engineering, University of Virginia, Charlottesville, VA, 22904, USA.
E-mail address: phopkins@virginia.edu (P.E. Hopkins).

https://doi.org/10.1016/j.carbon.2019.09.076
0008-6223/

serves as a mechanism to perturb the mass defect scattering term in well established phonon scattering models [12–14], allowing us to build-upon the current understanding of phonon defect interactions.

While there have been numerous investigations of ion implantation effects in diamond, a limited number have reported associated measured thermal conductivities, with most focusing on electron or neutron irradiation [15–17]. However, in the case of neutron irradiation, thermal conductivities as low as 71 W m^{-1} K^{-1} are reported for samples implanted at a dose of 4.5×10^{18} cm^{-2} [15]. A number of studies have investigated the role of point defects in diamond in the form of isotopic impurities, such as ^{13}C content in ^{12}C diamond crystals [10,18–21]. Among these studies, the thermal conductivity can be reduced by hundreds of W m^{-1} K^{-1} for isotopic impurity concentrations less than 1%, demonstrating the strong influence of impurity scattering on the thermal conductivity of the lattice. In this study, at the highest dose, we ultimately find the implanted mass impurity concentration to be much lower than 1% within the regions measured, but in combination with other forms of residual lattice defects generated during the implantation procedure, these defects are capable of reducing the thermal conductivity by two orders of magnitude.

In short, ion implantation is a bombardment procedure in which ionized atoms are accelerated into a target material. In industry, it is a fundamental process used in the manufacture of transistors and integrated circuits, traditionally utilized to implant semiconductors with acceptor or donor dopants [22,23]. However, ion implantation is also capable of producing material modification in the form of surface modification or amorphous layer formation [24,25]. A simple schematic of the process is represented in Fig. 1. Prior to implantation, the target, in this case diamond, maintains the periodicity of its lattice as a polycrystalline material. Upon bombardment of the lattice, ions of C^{3+}, N^{3+}, or O^{3+} are accelerated into the lattice at an energy of 16.5 MeV. At some point during the implant, the accelerated ions will come into contact with an atom at rest, and transfer a portion of the kinetic energy, creating what is known as a primary knock-on atom, which will in turn collide with another atom at rest [26]. Throughout the implantation, this process will happen repeatedly, yielding recoil cascades within the lattice, potentially generating high degrees of damage. When the accelerated ions no longer have sufficient energy to move a lattice atom from its equilibrium position, it comes to rest at its projected range. With doses and energies high enough, an amorphous layer will be produced at the end of range [27–29] with residual damage remaining above this layer in the form of point defects including vacancies, interstitials, substitutional impurities, as well as extended defects such as vacancy clusters. In this manuscript, we quantify the role of this residual damage in the layer above the end of range on the thermal conductivity of ion irradiated diamond.

2. Experimental

2.1. Sample fabrication and SRIM

Polycrystalline diamond substrates (with grain sizes extending up to 65–75% of the sample thickness) were purchased from Element Six and laser diced into quarters, yielding dimensions of 5 mm × 5 mm in area and 0.3 mm in thickness. Polycrystalline substrates were selected due to their prevalence in high-power heat-sink applications [2,30]. Samples were then implanted, normal to the surface, at Sandia National Laboratories with either C^{3+}, N^{3+}, or O^{3+} ions at a beam energy of 16.5 MeV using a 6 MV Tandem Van de Graaf accelerator. Fluences of 4×10^{14}, 4×10^{15}, and 4×10^{16} cm^{-2} were used for each ion, yielding a total of nine implanted samples. To ensure spatial uniformity of the implant, the beam was rastered across the sample surface during the implantation.

To estimate the longitudinal projected range of implantation depth, simulations were performed with Stopping and Range of Ions in Matter (SRIM) software. SRIM is a widely accepted Monte Carlo simulation software capable of modeling a number of features related to ion implantation including implant depths and concentrations on scales that would be prohibitively large for other modeling techniques such as molecular dynamics, for example [31,32]. We utilize detailed calculations with full damage cascades to predict damage profiles following implantation at a beam energy of 16.5 MeV for each ion. In each case, we specify the beam energy as 16.5 MeV and diamond substrate density as 3.515 g/cm^3 [33]. We utilize an average displacement energy of 37.5 eV [34,35], a lattice binding energy of 7.5 eV [36–38], and a surface binding energy of

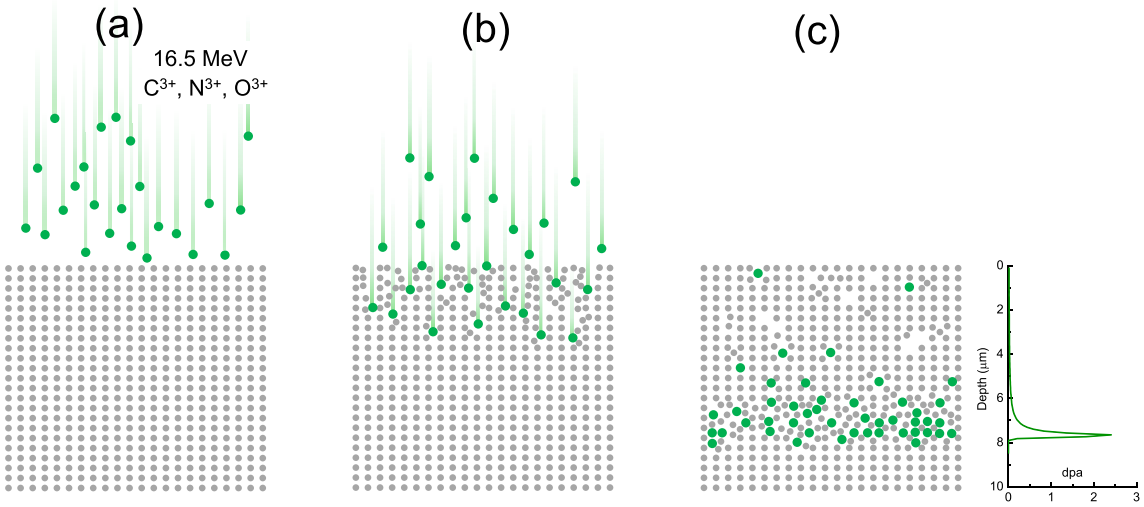

Fig. 1. Visualization of ion implantation. Prior to bombardment of the accelerated ions (a), the substrate maintains a diamond cubic crystal structure. Upon impingement of the lattice (b), the kinetic energy of the accelerated ions is transferred to the carbon atoms at rest, which become primary knock-on atoms, and are then launched further into the lattice until collision with other atoms at rest. This process repeats to create recoil cascades. Following implantation (c), the ions come to rest at the projected range, creating an amorphous region, and above this layer, leave behind both point and extended defects.

3.69 eV [39,40]. The output of the ion distribution and damage event calculations are combined in Fig. 2. The vacancy output of the damage event calculations are used to calculate the displacements per atom (dpa), assuming an atomic density of 1.77×10^{23} atoms cm^{-3} [41], and a fluence of 4×10^{16} cm^{-3}.

2.2. Structural characterization

To experimentally determine the range of damage in the implanted samples, an FEI Titan is used to perform scanning transmission electron microscopy (STEM). Fig. 3(a)-(c) display the results of the STEM measurements for each ion after exposure to a fluence of 4×10^{16} cm^{-2}. In both the SRIM simulations and STEM measurements, we find C^{3+}, the ion with the lowest atomic mass, to have the highest longitudinal projected range and depth of peak damage along with the lowest dpa. Conversely, O^{3+}, the ion with the highest atomic mass, produces the highest dpa but has the lowest longitudinal projected range and depth of peak damage. In general, the experimentally determined depth of peak damage for each ion is also found to be larger than those estimated through SRIM. We note that while SRIM is a widely used simulation tool within the ion implantation community, the quantitative results provide for a first order approximation of the actual projected range [42–44]. For instance, the crystal structure is not taken into account as a SRIM parameter, nor potential changes in composition of the target as a consequence of the implantation process. However, to obtain the most accurate results, we utilize detailed calculations with full damage cascades, and adjust the surface binding energy, lattice binding energy, and displacement energy of the diamond target to reflect those provided in the literature. To provide a comparison of the ranges found via experiment and simulation, we tabulate the results in Table 1.

To assess the structure of the diamond, we employ selected area diffraction (SAD). As shown in Fig. 3(d), non-diffracting regions approximately 5–9 μm beneath the sample surface are evident, suggesting the presence of an amorphous layer. Outside of this layer, diffraction is observed, demonstrating crystallinity of the material. We designate the center of the amorphous region as the longitudinal projected range of the ion, which corresponds to the point of highest damage shown in Fig. 2.

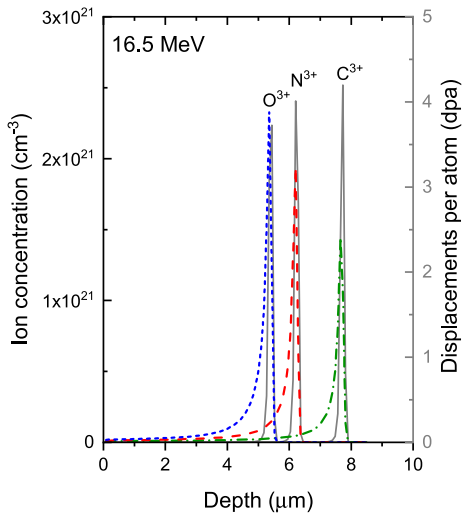

Fig. 2. SRIM calculations of ion concentrations (solid lines) as well as dpa as a function of depth for C^{3+}, N^{3+}, and O^{3+} (dashed and/or dotted textured lines). For each case, detailed calculations with full damage cascades were performed. The dpa is calculated from SRIM vacancy outputs assuming using a dose of 4×10^{16} cm^{-2}, an energy of 16.5 MeV, and atomic density of 1.77×10^{23} atoms cm^{-3} [41].

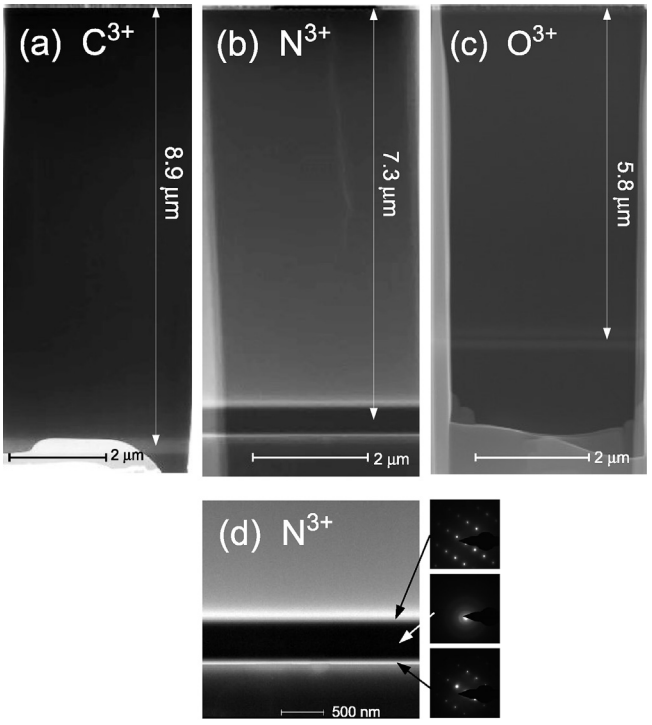

Fig. 3. (a) - (c) cropped STEM images for diamond samples implanted with ion of C^{3+}, N^{3+}, and O^{3+}, respectively, at a fluence of 4×10^{16} cm^{-2}. The depth from the sample surface to the center of the amorphous region is tabulated in Table 1. (d) Higher resolution STEM of the N^{3+} sample at the region of highest damage; amorphicity is demonstrated from the lack of diffraction via SAD measurements. The presence of diffraction confirms crystallinity immediately outside of the region of highest damage.

For insight on strain within the material, we employ high resolution x-ray diffraction (HRXRD). Triple axis measurements were performed with a Jordan Valley (Bruker) D1 diffractometer, utilizing Cu K α_1 radiation. For all samples, $2\theta : \omega$ summary scans reveal the presence of (111) and, at lower intensity, (311) reflections. Triple axis scans of the (111) peak demonstrate the presence of strain within the irradiated materials, as shown in Fig. 4(a) for all samples implanted at 4×10^{16} cm^{-2}. The peak to the lower angle of the (111) peak is indicative of strain within the material, caused by lattice damage as a result of the ion irradiation [23,45,46]. In samples implanted at a lower dose (4×10^{14}, 4×10^{15} cm^{-2}), the strain was found to be lower than the detection limit, which is expected, as the level of damage between doses varies by an order of magnitude. For comparison, Fig. 4(a) displays diamond implanted with C^{3+} at a dose of 4×10^{15} cm^{-2}, and does not display a strain shoulder to the lower angle of the (111) peak.

While the triple axis scans demonstrate the presence of strain within the samples, we also employ Bruker RADS simulation software [47] to gain quantitative insight into sample strain as a function of depth. In short, RADS software is a dynamical x-ray diffraction modeling software allowing for calculation of a number of parameters, including strain within thin films and crystalline materials. We utilize RADS to model the (111) peak of the 4×10^{16} cm^{-2} implanted samples; carbon implanted at 4×10^{16} cm^{-2} is displayed as an example in Fig. 4(b and c), which demonstrates the formation of a strained layer. A similar result was obtained for the nitrogen implanted sample, however, the strain layer intensity was insufficient to adequately model the oxygen implanted sample (see supplementary data). Due to diamond's low scattering factor, simulations were insensitive to the thickness of the diamond prior to the end of range, and therefore the precise

Table 1
Comparison of ion and peak dpa ranges as calculated with SRIM modeling software against experimentally observed values. The average measured range displays the distance measurement from STEM of the sample surface to the center of the amorphous region. The peak dpa values are calculated from SRIM and display the distance from the sample surface to the point of highest calculated dpa. In a similar manner, the longitudinal projected range values from SRIM display the calculated distance from the sample surface to the point of highest implanted ion concentration.

Ion	Average measured range (μm)	Peak dpa (μm)	Longitudinal projected range (μm)
C^{3+}	8.9	7.65	7.74
N^{3+}	7.3	6.21	6.21
O^{3+}	5.8	5.36	5.44

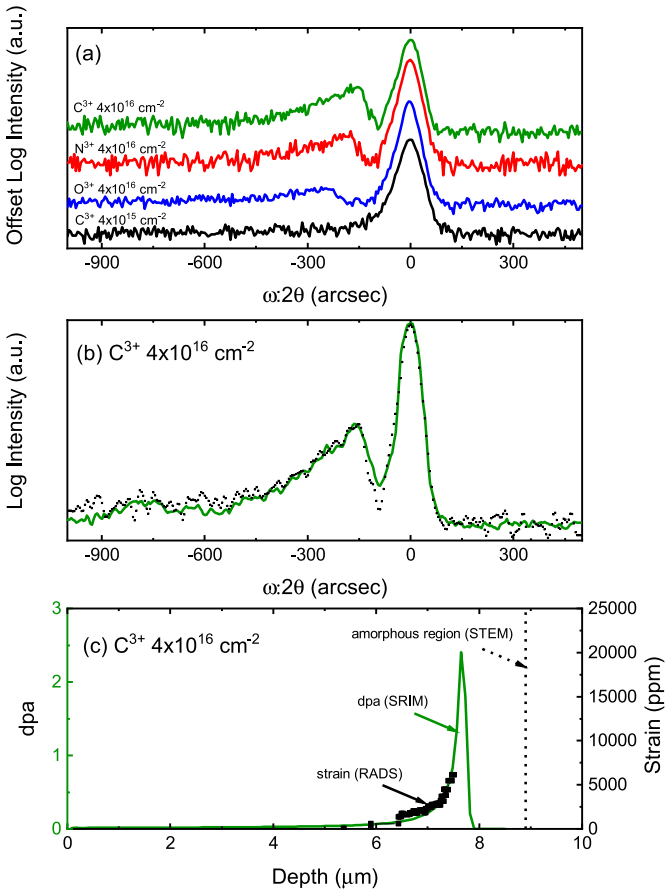

Fig. 4. (a) $\omega:2\theta$ HRXRD measurements of the (111) peak of the samples implanted at the highest dose ($4\times10^{16}\,cm^{-2}$). For comparison, diamond implanted with C^{3+} at $4\times10^{15}\,cm^{-2}$ is shown, displaying an absence of the satellite peak. (b) $\omega:2\theta$ measurement of the $4\times10^{16}\,cm^{-2}$ C^{3+} sample (black squares), which is modeled with RADS software (solid green line). The corresponding RADS simulation of the strain as a function of dose is shown in (c), which is plotted along with the SRIM results of the dpa, demonstrating similarity between the strain and dpa profile. The depth of the amorphous region, as measured by STEM, is displayed by the dashed black line. (A colour version of this figure can be viewed online.)

location of peak strain could not be determined from dynamical modeling. However, the profile of the strain is found to correspond with the dpa profile found through SRIM modeling: prior to the longitudinal projected range, the strain is maximized, in shallower regions, the strain is below the detection limit. Furthermore, for samples implanted at doses below $4\times10^{16}\,cm^{-2}$ strain levels are also beneath the detectable limit.

2.3. Thermal conductivity measurements

Following implantation, all samples were cleaned with an alcohol sonication (5 min sonication in isopropanol, acetone, and methanol, respectively) as well as a 30 min O_2 plasma clean to remove surface contaminants. O_2 plasma cleaning has been found particularly effective at removing carbon contamination attributed to vacuum pump operation in implantation procedures [48–50], and is additionally capable of etching an uncontaminated surface. However, we note that in this study, thermal conductivity measurements are representative of a region extending several microns beyond the surface, and can be decoupled from the thermal boundary conductance at the diamond surface, as discussed in the following section. Following cleaning, samples were coated with an 80 nm aluminum layer via electron beam evaporation to prepare them for thermal property measurements via time-domain thermoreflectance (TDTR). In summary, TDTR is a laser-based pump-probe technique that produces an oscillatory heating event at the surface of a sample, which in turn yields a corresponding change in the reflectivity, measured with a photodetector. An ultrafast Ti:Sapphire pulsed laser is used as the heat source, which enables fine temporal resolution of the thermal decay. We utilize a repetition rate of 80 MHz, a central wavelength of 800 nm, and spot sizes of 18 and 7.3 μm in diameter, respectively, for the pump and probe beams. The thermal properties of the samples were measured by fitting the ratio of the in-phase to out-of-phase lock-in signal to a thermal model which has been thoroughly detailed in the literature [51–54]. In this model, we consider the sample to consist of two layers: the 80 nm aluminum transducer followed by the ion implanted diamond, which we treat as a semi-infinite medium. Each layer of the sample is assigned three parameters: volumetric heat capacity (C_v), thermal conductivity (κ), and thickness (d). Between layers, the thermal boundary conductance, (h), produces an additional unknown [55].

3. Results and discussion

3.1. Thermal conductivity

The results of the TDTR measurements of the implanted samples are contrasted with an unirradiated sample in Fig. 5(a). For the unirradiated diamond, the thermal conductivity is measured to be $1996\pm213\,W\,m^{-1}\,K^{-1}$, which is in range of other reported CVD grown polycrystalline diamond thermal conductivities [56–58]. Following implantation, there is a significant decrease in thermal conductivity; at the lowest dose of $4\times10^{14}\,cm^{-2}$, the thermal conductivity is reduced by an approximate factor of 3, ranging from 718 to $599\,W\,m^{-1}\,K^{-1}$, depending on the species of implanted ion. As the dose is increased, there is a corresponding reduction in thermal conductivity, which is reduced to as low as $23.7\,W\,m^{-1}\,K^{-1}$ in the case of diamond implanted with O^{3+} at a dose of $4\times10^{16}\,cm^{-2}$. Furthermore, the thermal conductivity is found to scale with the mass of the implanted ion; C^{3+} implanted samples retain the highest overall thermal conductivity, whereas O^{3+} implanted samples display the largest reduction in thermal conductivity.

As previously mentioned, while numerous studies have investigated the results of ion implantation in diamond, few have also

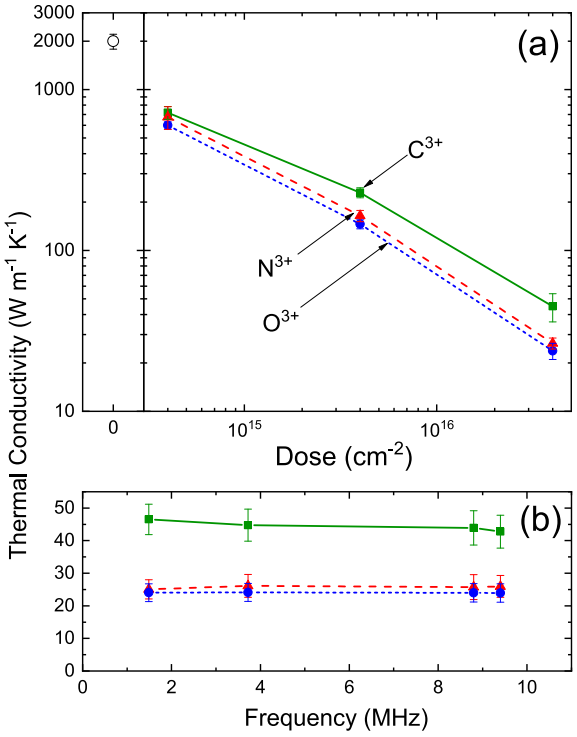

Fig. 5. Thermal conductivity of the implanted diamond samples as a function of implantation dose. The data displayed in (a) were measured using a modulation frequency of 8.8 MHz, where the data in (b) display the thermal conductivity of the 4×10^{16} cm^{-2} implanted samples measured over a modulation frequency range spanning 1.49–9.4 MHz. The error bars of the measurements account for measurement repeatability as well as uncertainty in the aluminum transducer thickness.

reported the corresponding reduction in thermal conductivity. In a study investigating the correlation of optical absorption to thermal conductivity in diamond [15], the thermal conductivity is reported for samples irradiated with neutrons, which reduced the thermal conductivity of the diamond from over 2100 W m^{-1} K^{-1}–71 W m^{-1} K^{-1} at the highest dose of 4.5×10^{18} W m^{-1} K^{-1}. For C^{3+}, N^{3+}, and O^{3+}, we observe larger reductions in the thermal conductivity. Such a result is expected as implant ions of larger mass are known to yield larger reductions in thermal conductivity [46].

As the damage produced through implantation spatially varies with depth, the depths thermally probed with TDTR are insightful when analyzing the results. The modulation frequency of the pump is of particular importance, and has been noted in other works focused upon the thermal conductivity of irradiated materials [46,55], as it directly influences the penetration depth of the measurement. While the measurements in Fig. 5(a) were taken at 8.8 MHz, the effects of modulation frequency are investigated by measuring the thermal conductivity of the samples implanted at the highest dose for a number of frequencies spanning 1.49–9.4 MHz. However, as the measured thermal conductivities are within error for each ion species, we observe no dependence upon the modulation frequency.

Although there is no observed change in thermal conductivity within the range of applied modulation frequencies, as shown in Fig. 5(b), it remains an important feature of the analysis to understand the depth probed by the measurement. To a first approximation, the thermal penetration depth, δ, which represents the $1/e$ temperature decay used in the analysis of TDTR data, can be approximated as

$$\delta = \sqrt{\frac{\kappa}{\pi C_v f}}, \quad (1)$$

where κ is the thermal conductivity of the material of interest, C_v is volumetric heat capacity, and f is the modulation frequency of the pump [59]. While this calculation can provide a reasonable approximation of the thermal penetration depth, we utilize a more accurate approach to calculate δ, discussed in detail by Braun et al. [60,61], which accounts for effects of the transducer, pump and probe spot size, and the interface between the transducer and substrate.

To visualize the depths thermally probed with TDTR, we calculate representative temperature distributions for the C^{3+} implanted samples, shown in Fig. 6(a)–(c). For each calculation, we apply the same parameters used in the thermal response model for TDTR analysis: an 8.8 MHz modulated pump beam impinging upon an 80 nm aluminum transducer with a thermal conductivity of 98 W m^{-1} K^{-1}, and volumetric heat capacity of 2.43 MJ m^{-3} K^{-1}, followed by a defected diamond substrate with a volumetric heat capacity of 1.78 MJ m^{-3} K^{-1} [62–65] and measured thermal conductivity of 718, 229, or 44.8 W m^{-1} K^{-1}, depending on the sample. In general, it can be seen in all cases that the vast majority of the associated temperature rise is dispersed within the aluminum transducer. As the thermal conductivity is decreased, there is greater diffusion of heat into the substrate, and therefore, slightly larger depths are represented in the measurement. For reference, the $1/e$ thermal penetration depth calculated via Equation (1) is represented in Fig. 6(a)–(c) by the vertical dotted line. We find this calculated thermal penetration depth to be 3.82, 2.16, and 0.95 μm for the 4×10^{14}, 4×10^{15}, and 4×10^{16} cm^{-2} implanted samples, respectively. In contrast, the $1/e$ penetration depth for the same samples is calculated with the exact solution as 0.09, 0.65, and 0.70 μm. As mentioned previously, the disparity between the two calculations arises from the fact that Equation (1) does not take into consideration the size of the pump or probe, nor the transducer layer and the corresponding thermal boundary conductance across the transducer/substrate interface (i.e., Al/diamond). In reality, there is a high degree of radial heat dissipation in the aluminum transducer, which reduces the thermal penetration depth that would be expected from Equation (1) [61].

In addition to the two dimensional temperature profile of the carbon implanted samples, we calculate the cross-plane temperature profile for all samples at the radial center of the pump. This profile is shown as a normalized temperature rise in Fig. 6(d)–(e) and non-normalized in Fig. 6(g)–(i) (assuming a pump power of 30 mW) to provide reference for the magnitude of the temperature rise induced by TDTR. The range is plotted on a log scale to more easily observe trends along the depth of the sample. In all cases, there is a temperature drop at the interface of the transducer and diamond substrate followed by a temperature decay spanning approximately 10 μm.The degree of the temperature drop between the transducer and substrate is generally attributed to the thermal boundary conductance of the interface but is also affected by the thermal conductivity of the substrate. This is demonstrated here, as a thermal boundary conductance of 150 MW m^{-2} K^{-1} is applied to all samples, yet a difference in temperature drop at the interface is observed depending on the thermal conductivity. The thermal boundary conductance, G, can be expressed as $G = Q/\Delta T$, where Q is the applied heat flux and ΔT is the temperature change across the interface. As G is constant for each case, differences in ΔT can be attributed to changes in Q due to greater radial heat spreading within the aluminum transducer [60]. The total depth at which a temperature rise is induced by the pump pulse is proportionally related to the thermal conductivity such that samples implanted at

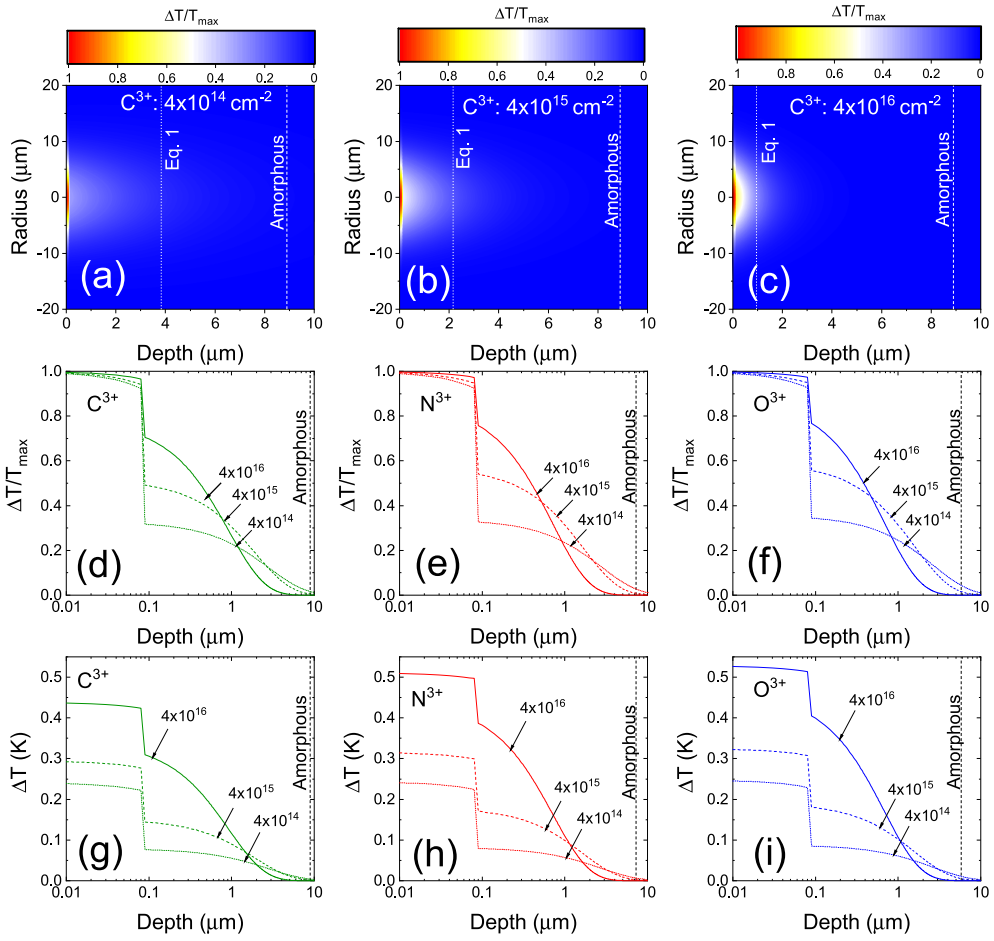

Fig. 6. (a) - (c) display the normalized two dimensional temperature distribution of the C^{3+} implanted diamond at 4×10^{14}–4×10^{16} cm^{-2}. The depth of the amorphous region is represented by the dashed line, and for reference, the 1/*e* thermal penetration depth, as calculated by Equation (1), is displayed by the dotted line. (d)–(f) display the normalized temperature profile in the cross-plane direction, at the center of the pump radius for all samples and doses, which is also non-normalized in (g)–(i) for a pump power of 30 mW. All figures are of the temperature profile induced 100 ps following the impingement of the pump pulse.

the lowest dose are probed furthest by the applied temperature rise. However, even in the case of O^{3+} implanted diamond, which produced an amorphous region 5.8 μm from the surface, only 4% of the temperature rise produced at the sample surface is capable of penetrating to the amorphous band, and therefore the measurement has negligible sensitivity to the region.

3.2. Sampled defect concentration

The generally accepted thermal penetration depth, or the depth at which the induced temperature rise falls to 1/*e* of that of the surface, is plotted as a function of dose for all samples in Fig. 7(a). In this case, it is found that the 1/*e* depth generally increases with dose, but is less than 1 μm, in all cases. STEM demonstrates that amorphous regions are produced 5.8–8.9 μm beneath the surface. Furthermore, SRIM calculations demonstrate very small ion concentrations and displacements within 1 μm of the surface. To estimate the degree of general damage probed by the measurement relative to the total amount of damage within the implanted samples, we integrate the dpa profiles of SRIM from the surface of the sample to the 1/*e* thermal penetration depth, then divide this value by the integration of the entire dpa profile. Fig. 7(b) displays the results of the calculation, which demonstrates that even in the case of high dose implants (4×10^{16} cm^{-2}), only 1% of the total dpa is probed by the TDTR measurement. Furthermore, we note that

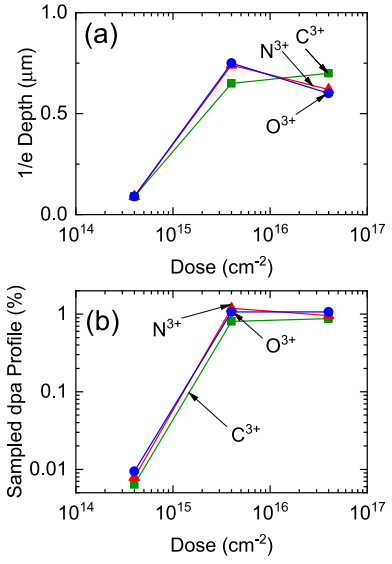

Fig. 7. (a) 1/*e* thermal penetration depths calculated for each ion as a function of dose. (b) Percentages of the dpa profile thermally probed by TDTR, which is calculated by taking the ratio of the total integrated area of the dpa profile to the profile integrated from the surface to the 1/*e* thermal penetration depth.

this calculation would provide for a slight overestimation of the actual percentage of sampled dpa profile, as STEM measurements demonstrate that the peak of the damage profile is shifted slightly further into the sample than is calculated in SRIM. We apply this same integration procedure for the ion concentrations probed by the measurement, however, for all ion species, the implant concentrations at depths less than 1 μm are reported as zero in SRIM, as they are much less than the concentrations found at the projected range, which suggests that the sampled volumetric ion concentrations are correspondingly much less than 1%.

In addition to the implanted ion concentration and dpa profile, localized strain has also been demonstrated as subject to changes in ion dose [23,66–69]. This is also demonstrated in the present study, as satellite peak formation is not observed in HRXRD measurements for doses lower than $4 \times 10^{16}\,cm^{-2}$ (Fig. 4(a)). However, as determined from dynamical diffraction simulations of the measurements, the induced strain within the implanted samples is found to be similar in profile to the dpa, and is beneath the detectable limit in the region thermally probed. In a prior study investigating phonon scattering within single crystal silicon wafers self implanted with various isotopes of silicon at 3.75 MeV [46], localized strain was found to provide a key source of phonon scattering. However, the strain per defect was found to decrease with increased ion fluence, corresponding with the formation of extended defects, and is also probable in the current study, as extended defect formation, including the formation of vacancy clusters, has been previously demonstrated in diamond targets subjected to electron or ion irradiation[70–72].

An additional form of extended defect prevalent in irradiated crystals implanted with heavy ions of sufficiently high energy is the formation of ion tracks, or voids, within the lattice left in the path of incident ions or recoiling knock-on atoms. In a recent work by Abdullaev et al. [27], bright field cross sectional TEM imaging was used to demonstrate the clear formation of latent ion tracks left behind in sapphire crystals implanted with Xe ions at 167 MeV before culminating in an amorphous band at the end of range. While the formation of amorphous layers is also demonstrated in the present study, diamond is known for its resistance to the formation of latent tracks [73,74], and there is limited evidence of their formation in either experimental or computational studies [75]. Even for heavy ion implantation including $Au^{+}$and Ag^{+} at ion energies up to 130 MeV, latent track formation is not observed [76]. As the samples in the present study are implanted with lighter ions and at a lower energy, there is no expected contribution to the thermal conductivity reduction from latent ion tracks.

4. Conclusions

In summary, we report on the measured thermal conductivity reduction of diamond samples irradiated with C^{3+}, N^{3+}, and O^{3+} ions with a beam energy of 16.5 MeV, and fluences ranging from 4×10^{14} to $4 \times 10^{16}\,cm^{-2}$. The irradiation produced amorphous regions within the samples at depths ranging from 5.8 to 8.9 μm. Through time-domain thermoreflectance, reductions in thermal conductivity were found to trend with the mass of the implant ion, and span two orders of magnitude, decreasing the thermal conductivity from nearly $2000\,W\,m^{-1}\,K^{-1}$ to approximately $20\,W\,m^{-1}\,K^{-1}$ at the highest dose. HRXRD analysis in combination with dynamical diffraction simulations reveal the formation of a strained layer in the samples implanted at a dose of $4 \times 10^{16}\,cm^{-2}$, which is similar in profile to the dpa calculated through SRIM simulations, and is maximized prior to the amorphous region. Thermal penetration depth calculations demonstrate that TDTR measurements thermally probe the regions above this amorphous band where the samples maintain a polycrystalline structure and the sample strain is below detectable limits of HRXRD techniques. Furthermore, within these regions, mass impurity concentrations are found to be much less than 1%. In spite of these low concentrations, however, the degree of high frequency phonon defect scattering is found to be sufficient to yield orders of magnitude reductions in the measured thermal conductivity, demonstrating the remarkably large impact of dilute levels of defects induced through ion beam modification.

Declaration of competing interest

The authors declare that they have no known competing financial interests or personal relationships that could have appeared to influence the work reported in this paper.

Acknowledgements

The authors would like to thank D. Buller for his assistance in the implantation. This material is based upon work supported by the Air Force Office of Scientific Research under award number FA9550-18-1-0352. We appreciate support from the Office of Naval Research through a MURI program, Grant No. N00014-18-1-2429. This work was performed, in part, at the Center for Integrated Nanotechnologies, an Office of Science User Facility operated for the U.S. Department of Energy (DOE) Office of Science. Sandia National Laboratories is a multimission laboratory managed and operated by National Technology & Engineering Solutions of Sandia, LLC, a wholly owned subsidiary of Honeywell International, Inc., for the U.S. DOE's National Nuclear Security Administration under contract DE-NA-0003525. The views expressed in the article do not necessarily represent the views of the U.S. DOE or the United States Government.

Appendix A. Supplementary data

Supplementary data to this article can be found online at https://doi.org/10.1016/j.carbon.2019.09.076.

References

[1] V. Goyal, A.V. Sumant, D. Teweldebrhan, A.A. Balandin, Direct low-temperature integration of nanocrystalline diamond with GaN substrates for improved thermal management of high-power electronics, Adv. Funct. Mater. 22 (7) (2012) 1525–1530, https://doi.org/10.1002/adfm.201102786.
[2] D. Liu, D. Francis, F. Faili, C. Middleton, J. Anaya, J.W. Pomeroy, D.J. Twitchen, M. Kuball, Impact of diamond seeding on the microstructural properties and thermal stability of GaN-on-diamond wafers for high-power electronic devices, Scr. Mater. 128 (2017) 57–60, https://doi.org/10.1016/j.scriptamat.2016.10.006.
[3] D. Francis, J. Wasserbauer, F. Faili, D. Babic, F. Ejeckam, W. Hong, P. Specht, E. Weber, GaN-HEMT epilayers on diamond substrates: recent progress, in: CS MANTECH Conference, 2007, p. 133, https://doi.org/10.1109/LED.2007.908490.
[4] D. Dumka, D. Francis, T. Chou, F. Ejeckam, F. Faili, AlGaN/GaN HEMTs on diamond substrate with over 7 W/mm output power density at 10 GHz, Electron. Lett. 49 (20) (2013) 1298–1299, https://doi.org/10.1049/el.2013.1973.
[5] J.D. Blevins, G.D. Via, K. Sutherlin, S. Tetlak, B. Poling, R. Gilbert, B. Moore, J. Hoelscher, B. Stumpff, A. Bar-Cohen, J.J. Maurer, A. Kane, Recent progress in GaN-on-diamond device technology, CS MANTECH 2014, in: 2014 International Conference on Compound Semiconductor Manufacturing Technology, 2014, pp. 105–108. URL, http://www.scopus.com/inward/record.url?eid=2-s2.0-84906536351{%}7B{&}{%}7DpartnerID=tZOtx3y1.
[6] G.A. Slack, Nonmetallic crystals with high thermal conductivity, J. Phys. Chem. Solids 34 (2) (1973) 321–335, https://doi.org/10.1016/0022-3697(73)90092-9.
[7] R. Berman, F.E. Simon, J.M. Ziman, The thermal conductivity of diamond at low temperatures, Proc. R. Soc. A Math. Phys. Eng. Sci. 220 (1141) (1953) 171–183, https://doi.org/10.1098/rspa.1953.0180.
[8] G.A. Slack, Thermal conductivity of pure and impure silicon, silicon carbide, and diamond, J. Appl. Phys. 35 (12) (1964) 3460–3466, https://doi.org/10.1063/1.1713251.

[9] W. Vandersande, Thermal conductivity of diamond between 170 and 1200 K and the isotope effect, Phys. Rev. B 47 (22) (1993) 14850.

[10] L. Wei, P.K. Kuo, R.L. Thomas, T.R. Anthony, W.F. Banholzer, Thermal conductivity of isotopically modified single crystal diamond, Phys. Rev. Lett. 70 (24) (1993) 3764–3767, https://doi.org/10.1103/PhysRevLett.70.3764.

[11] T. Zhu, K. Swaminathan-Gopalan, K.J. Cruse, K. Stephani, E. Ertekin, Vibrational energy transport in hybrid ordered/disordered nanocomposites: hybridization and avoided crossings of localized and delocalized modes, Adv. Funct. Mater. 28 (17) (2018), https://doi.org/10.1002/adfm.201706268, 1706268.

[12] P.G. Klemens, The scattering of low-frequency lattice waves by static imperfections, Proc. Phys. Soc. Sect. A 68 (12) (1955) 1113–1128, https://doi.org/10.1088/0370-1298/68/12/303.

[13] B. Abeles, Lattice thermal conductivity of disordered semiconductor alloys at high temperatures, Phys. Rev. 131 (5) (1963) 1906–1911, https://doi.org/10.1103/PhysRev.131.1906.

[14] G. Shrivastava, The Physics of Phonons, Taylor & Francis Group, LLC, New York, 1990.

[15] D.T. Morelli, Correlating optical absorption and thermal conductivity in diamond, Appl. Phys. Lett. 63 (2) (2000) 165–167.

[16] C. Uher, D.T. Morelli, Influence of neutron irradiation on the thermal conductivity of vapor-deposited diamond, J. Appl. Phys. 76 (3) (1994) 1515–1517, https://doi.org/10.1063/1.357727.

[17] J.W. Vandersande, Thermal-conductivity reduction in electron-irradiated type-II a diamonds at low temperatures, Phys. Rev. B 15 (4) (1977) 2355–2362, https://doi.org/10.1103/PhysRevB.15.2355.

[18] R.E. Jones, A.M. Toxen, Thermal conductivity of pure indium, Phys. Rev. 120 (4) (1960) 1167–1170, https://doi.org/10.1103/PhysRev.120.1167.

[19] T.R. Anthony, J.L. Fleischer, J.R. Olson, D.G. Cahill, The thermal conductivity of isotopically enriched polycrystalline diamond films, J. Appl. Phys. 69 (12) (1991) 8122–8125, https://doi.org/10.1063/1.347463.

[20] J.R. Olson, R.O. Pohl, J.W. Vandersande, A. Zoltan, T.R. Anthony, W.F. Banholzer, Thermal conductivity of diamond between 170 and 1200 K and the isotope effect, Phys. Rev. B 47 (22) (1993) 14850–14856, https://doi.org/10.1103/PhysRevB.47.14850.

[21] D.G. Onn, A. Witek, Y.Z. Qiu, T.R. Anthony, W.F. Banholzer, Some aspects of the thermal conductivity of isotopically enriched diamond single crystals, Phys. Rev. Lett. 68 (18) (1992) 2806–2809, https://doi.org/10.1103/PhysRevLett.68.2806.

[22] J. Wood, Ion implantation, in: K.H.J. Buschow, R.W. Cahn, M.C. Flemings, B. Ilschner, E.J. Kramer, S. Mahajan, P. Veyssière (Eds.), Encyclopedia of Materials: Science and Technology, Elsevier, Oxford, 2001, pp. 4284–4286. https://doi.org/10.1016/B0-08-043152-6/00751-8.

[23] C. Moulet, M. Goorsky, Ion implantation, in: M. Goorsky (Ed.), Ion Implantation, InTech, Rijeka, 2012, pp. 65–89. Ch. Lattice St.

[24] J.M. Poate, G. Foti, D.C. Jacobson, Surface Modification and Alloying: by Laser, Ion, and Electron Beams, vol. 8, Springer Science & Business Media, 2013.

[25] G.G. Fuentes, Chapter 20 - surface engineering and micro-manufacturing, in: Y. Qin (Ed.), Micromanufacturing Engineering and Technology, second ed., Micro and Nano Technologies, William Andrew Publishing, Boston, 2015, pp. 459–486. https://doi.org/10.1016/B978-0-323-31149-6.00020-7.

[26] K. Whittle, Radiation damage, 2, in: Nuclear Materials Science, IOP Publishing, 2016, pp. 2053–2563, https://doi.org/10.1088/978-0-7503-1104-5ch2.

[27] A. Abdullaev, B. Muminov, J. O'Connell, V.A. Skuratov, V.S. Chauhan, M. Khafizov, Z.N. Utegulov, Thermal Transport Across Nanoscale Damage Profile in Sapphire Irradiated by Swift Heavy Ions: Picosecond Time Domain Thermoreflectance, Available at SSRN, https://ssrn.com/abstract=3378386, April 26, 2019.

[28] S. Prussin, D. Margolese, R. Tauber, Formation of amorphous layers by ion implantation, J. Appl. Phys. 57 (1985) 180, https://doi.org/10.1016/0168-583X(85)90415-X.

[29] G. Carter, W. Grant, Amorphisation of solids by ion implantation, Nucl. Instrum. Methods 199 (1982) 17, https://doi.org/10.1130/MEM156-p1.

[30] T. Liu, D. Raabe, W. Mao, S. Zaefferer, Microtexture and grain boundaries in freestanding CVD diamond films: growth and twinning mechanisms, Adv. Funct. Mater. 19 (24) (2009) 3880–3891, https://doi.org/10.1002/adfm.200901231.

[31] J.F. Ziegler, M.D. Ziegler, J.P. Biersack, SRIM - the stopping and range of ions in matter, Nucl. Instrum. Methods Phys. Res. Sect. B Beam Interact. Mater. Atoms 268 (11–12) (2010) 1818–1823, https://doi.org/10.1016/j.nimb.2010.02.091, 2010.

[32] J.F. Ziegler, Srim-2003, Nucl. Instrum. Methods Phys. Res. Sect. B Beam Interact. Mater. Atoms 219–220 (1–4) (2004) 1027–1036, https://doi.org/10.1016/j.nimb.2004.01.208.

[33] J.C. Angus, H.A. Will, W.S. Stanko, Growth of diamond seed crystals by vapor deposition, J. Appl. Phys. 39 (6) (1968) 2915–2922, https://doi.org/10.1063/1.1656693, arXiv:arXiv:1011.1669v3.

[34] J. Koike, D.M. Parkin, T.E. Mitchell, Displacement threshold energy for type IIa diamond, Appl. Phys. Lett. 60 (12) (1992) 1450–1452, https://doi.org/10.1063/1.107267.

[35] B.M.J.C. Bourgoin, Threshold energy for atomic displacements in diamond, Phys. Rev. B 14 (8) (1976) 3690–3694, https://doi.org/10.1103/PhysRevB.14.3690.

[36] R.Q. Hood, P.R. Kent, R.J. Needs, P.R. Briddon, Quantum Monte Carlo study of the optical and diffusive properties of the vacancy defect in diamond, Phys. Rev. Lett. 91 (7) (2003), 076403, https://doi.org/10.1103/PhysRevLett.91.076403.

[37] P.R.C. Kent, M.D. Towler, R.J. Needs, G. Rajagopal, Carbon clusters near the crossover to fullerene stability, Phys. Rev. B Condens. Matter Mater. Phys. 62 (23) (2000) 15394–15397, https://doi.org/10.1103/PhysRevB.62.15394, arXiv:9909037.

[38] H. Shin, S. Kang, J. Koo, H. Lee, J. Kim, Y. Kwon, Cohesion energetics of carbon allotropes: quantum Monte Carlo study, J. Chem. Phys. 140 (2014), https://doi.org/10.1063/1.4867544doi.org/10.1063/1.4867544, 114702–114702.

[39] Y.S. Nechaev, T.N. Veziroglu, Thermodynamic aspects of the graphene/graphane/hydrogen systems: relevance to the hydrogen on-board storage problem, Adv. Mater. Phys. Chem. 3 (2013) 255–280, https://doi.org/10.4236/ampc.2013.35037.

[40] Y.S. Nechaev, V.P. Filippova, A. Yürüm, Y. Yürüm, T.N. Veziroglu, The reversible hydrogenation-dehydrogenation of membrane and epitaxial graphenes, J. Chem. Eng. Chem. Res 2 (1) (2015) 421–456.

[41] C.J. Torng, J.M. Sivertsen, Structure and bonding studies of the C : N thin films produced by rf sputtering method, J. Mater. Res. 5 (11) (2017) 2490.

[42] M. Nastasi, J.W. Mayer, Y. Wang, Ion Beam Analysis: Fundamentals and Applications, CRC Press, 2014.

[43] R.E. Stoller, M.B. Toloczko, G.S. Was, A.G. Certain, S. Dwaraknath, F.A. Garner, On the use of SRIM for computing radiation damage exposure, Nucl. Instrum. Methods Phys. Res. Sect. B Beam Interact. Mater. Atoms 310 (2013) 75–80, https://doi.org/10.1016/j.nimb.2013.05.008.

[44] H. Paul, A. Schinner, Judging the reliability of stopping power tables and programs for protons and alpha particles using statistical methods, Nucl. Instrum. Methods Phys. Res. Sect. B Beam Interact. Mater. Atoms 227 (4) (2005) 461–470, https://doi.org/10.1016/j.nimb.2004.10.007.

[45] Y. Wang, T. Bai, C. Li, M.J. Tadjer, T.J. Anderson, J.K. Hite, M.A. Mastro, C.R. Eddy, K.D. Hobart, B.N. Feigelson, M.S. Goorsky, Defect characterization of multicycle rapid thermal annealing processed p-GaN for vertical power devices, ECS Journal of Solid State Science and Technology 8 (2) (2019) P70–P76, https://doi.org/10.1149/2.0011902jss.

[46] E.A. Scott, K. Hattar, C.M. Rost, J.T. Gaskins, M. Fazli, C. Ganski, C. Li, T. Bai, Y. Wang, K. Esfarjani, M. Goorsky, P.E. Hopkins, Phonon scattering effects from point and extended defects on thermal conductivity studied via ion irradiation of crystals with self-impurities, Physical Review Materials 2 (2018), 095001, https://doi.org/10.1103/PhysRevMaterials.2.095001.

[47] Bruker Corporation (2018).

[48] P.E. Hopkins, K. Hattar, T. Beechem, J.F. Ihlefeld, D.L. Medlin, E.S. Piekos, Reduction in thermal boundary conductance due to proton implantation in silicon and sapphire, Appl. Phys. Lett. 98 (23) (2011) 231901, https://doi.org/10.1063/1.3592822.

[49] P.E. Hopkins, K. Hattar, T. Beechem, J.F. Ihlefeld, D.L. Medlin, E.S. Piekos, Addendum: "Reduction in thermal boundary conductance due to proton implantation in silicon and sapphire, Appl. Phys. Lett. 101 (2012), 099903, https://doi.org/10.1063/1.3592822.

[50] C.S. Gorham, K. Hattar, R. Cheaito, J.C. Duda, J.T. Gaskins, T.E. Beechem, J.F. Ihlefeld, L.B. Biedermann, E.S. Piekos, D.L. Medlin, P.E. Hopkins, Ion irradiation of the native oxide/silicon surface increases the thermal boundary conductance across aluminum/silicon interfaces, Phys. Rev. B 90 (2014), 024301, https://doi.org/10.1103/PhysRevB.90.024301.

[51] A. Schmidt, Optical Characterization of Thermal Transport from the Nanoscale to the Macroscale, Dissertation, Massachusetts Institute of Technology, 2008. URL, http://hdl.handle.net/1721.1/44798.

[52] D.G. Cahill, Analysis of heat flow in layered structures for time-domain thermoreflectance, Rev. Sci. Instrum. 75 (12) (2004) 5119–5122, https://doi.org/10.1063/1.1819431.

[53] D.G. Cahill, K.E. Goodson, A. Majumdar, Thermometry and thermal transport in micro/nanoscale solid-state devices and structures, J. Heat Transf. 124 (2) (2002) 223, https://doi.org/10.1115/1.1454111.

[54] P.E. Hopkins, J.R. Serrano, L.M. Phinney, S.P. Kearney, T.W. Grasser, C.T. Harris, Criteria for cross-plane dominated thermal transport in multilayer thin film systems during modulated laser heating, J. Heat Transf. 132 (8) (2010), 081302, https://doi.org/10.1115/1.4000993.

[55] R. Cheaito, C.S. Gorham, A. Misra, K. Hattar, P.E. Hopkins, Thermal conductivity measurements via time-domain thermoreflectance for the characterization of radiation induced damage, J. Mater. Res. 30 (9) (2015) 1403–1412, https://doi.org/10.1557/jmr.2015.11.

[56] J. L. Braun, D. H. Olson, J. T. Gaskins, P. E. Hopkins, A steady-state thermoreflectance method to measure thermal conductivity, Rev. Sci. Instrum. 90 (2). doi:10.1063/1.5056182.

[57] C.M. Rost, J. Braun, K. Ferri, L. Backman, A. Giri, E.J. Opila, J.P. Maria, P.E. Hopkins, Hafnium nitride films for thermoreflectance transducers at high temperatures: potential based on heating from laser absorption, Appl. Phys. Lett. 111 (15) (2017), https://doi.org/10.1063/1.5006648, 151902.

[58] S.P.R. Clark, P. Ahirwar, F.T. Jaeckel, C.P. Hains, A.R. Albrecht, T.J. Rotter, L.R. Dawson, G. Balakrishnan, P.E. Hopkins, L.M. Phinney, J. Hader, J.V. Moloney, Growth and thermal conductivity analysis of polycrystalline GaAs on chemical vapor deposition diamond for use in thermal management of high-power semiconductor lasers, Journal of Vacuum Science & Technology B, Nanotechnology and Microelectronics: Materials, Processing, Measurement, and Phenomena 29 (3) (2011), 03C130, https://doi.org/10.1116/1.3565054.

[59] Y.K. Koh, S.L. Singer, W. Kim, J.M.O. Zide, H. Lu, D.G. Cahill, A. Majumdar, A.C. Gossard, Comparison of the 3 omega method and time-domain

thermoreflectance for measurements of the cross-plane thermal conductivity of epitaxial semiconductors, J. Appl. Phys. 105 (5) (2009), 054303, https://doi.org/10.1063/1.3078808.
[60] J.L. Braun, P.E. Hopkins, Upper limit to the thermal penetration depth during modulated heating of multilayer thin films with pulsed and continuous wave lasers: a numerical study, J. Appl. Phys. 121 (17) (2017), https://doi.org/10.1063/1.4982915, 175107.
[61] J. Braun, C. Szwejkowski, A. Giri, P. Hopkins, On the steady-state temperature rise during laser heating of multilayer thin films in optical pump-probe techniques, J. Heat Transf. 140 (May) (2017), 052801, https://doi.org/10.1115/1.4038713.
[62] J.E. Desnoyehs, J.A. Morrison, The heat capacity of diamond between 12· 8° and 277°k, Philos. Mag. 3 (25) (1958) 42–48, https://doi.org/10.1080/14786435808243223.
[63] K.S. Pitzer, The heat capacity of diamond from 70 to 300°K, J. Chem. Phys. 6 (2) (1938) 68–70, https://doi.org/10.1063/1.1750204.
[64] W. DeSorbo, Specific heat of diamond at low temperatures, J. Chem. Phys. 21 (5) (1953) 876–880, https://doi.org/10.1063/1.1699050.
[65] A.C. Victor, Heat capacity of diamond at high temperatures, J. Chem. Phys. 36 (7) (1962) 1903–1911, https://doi.org/10.1063/1.1701288.
[66] C. Miclaus, M.S. Goorsky, Strain evolution in hydrogen-implanted silicon, J. Phys. D Appl. Phys. 36 (2003) A177–A180, https://doi.org/10.1088/0022-3727/36/10A/336.
[67] S.T. Horng, M.S. Goorsky, Complete p-type activation in vertical-gradient freeze GaAs co-implanted with gallium and carbon, Appl. Phys. Lett. 68 (11) (1996) 1537–1539, https://doi.org/10.1063/1.115691.
[68] S. Hayashi, M. Goorsky, A. Noori, D. Bruno, Materials issues for the heterogeneous integration of III-V compounds, J. Electrochem. Soc. 153 (12) (2006) G1011, https://doi.org/10.1149/1.2353607.
[69] Y. Wang, T. Bai, C. Li, M.J. Tadjer, T.J. Anderson, J.K. Hite, M.A. Mastro, C.R. Eddy, K.D. Hobart, B.N. Feigelson, M.S. Goorsky, Defect characterization of multicycle rapid thermal annealing processed p-GaN for vertical power devices, ECS Journal of Solid State Science and Technology 8 (2) (2019) P70–P76, https://doi.org/10.1149/2.0011902jss.
[70] J. F. Prins, Ion implantation of diamond for electronic applications, Semicond. Sci. Technol. 18 (3). doi:10.1088/0268-1242/18/3/304.
[71] S. Dannefaer, W. Zhu, Vacancies in polycrystalline diamond films, Phys. Rev. B Condens. Matter Mater. Phys. 53 (4) (1996) 1979–1984, https://doi.org/10.1103/PhysRevB.53.1979.
[72] J.F. Prins, Ion-implanted structures and doped layers in diamond, Mater. Sci. Rep. 7 (7–8) (1992) 275–364, https://doi.org/10.1016/0920-2307(92)90001-H.
[73] U.A. Glasmacher, M. Lang, H. Keppler, F. Langenhorst, R. Neumann, D. Schardt, C. Trautmann, G.A. Wagner, Phase transitions in solids stimulated by simultaneous exposure to high pressure and relativistic heavy ions, Phys. Rev. Lett. 96 (19) (2006), https://doi.org/10.1103/PhysRevLett.96.195701, 195701.
[74] M. Lang, U.A. Glasmacher, R. Neumann, D. Schardt, C. Trautmann, G.A. Wagner, Energy loss of 50-GeV uranium ions in natural diamond, Appl. Phys. Mater. Sci. Process 80 (4) (2005) 691–694, https://doi.org/10.1007/s00339-004-3104-1.
[75] D. Schwen, E.M. Bringa, Atomistic simulations of swift ion tracks in diamond and graphite, Nucl. Instrum. Methods Phys. Res. Sect. B Beam Interact. Mater. Atoms 256 (1) (2007) 187–192, https://doi.org/10.1016/j.nimb.2006.12.001.
[76] D.S. Misra, U. Palnitkar, P.K. Tyagi, M.K. Singh, E. Titus, D.K. Avasthi, P. Vasa, P. Ayyub, Melting and defect generation in chemical vapor deposited diamond due to irradiation with 100 MeV Au+ and Ag+ ions, Thin Solid Films 503 (1–2) (2006) 121–126, https://doi.org/10.1016/j.tsf.2005.11.029.